Pressure-induced insulator-to-metal transition in the van der Waals compound $CoPS_3$

Takahiro Matsuoka,[1,*] Rahul Rao,[2] Michael A. Susner,[2] Benjamin S. Conner,[3,4] Dongzhou Zhang,[5,6] and David Mandrus[1,7,8,†]

[1]*Department of Materials Science and Engineering, University of Tennessee, Knoxville, Tennessee 37996, USA*
[2]*Materials and Manufacturing Directorate, Air Force Research Laboratory, Wright-Patterson Air Force Base, Ohio 45433, USA*
[3]*Sensors Directorate, Air Force Research Laboratory, Wright-Patterson Air Force Base, Ohio 45433, USA*
[4]*National Research Council, Washington DC 20001, USA*
[5]*Hawaii Institute of Geophysics and Planetology, University of Hawaii at Manoa, 1680 East-West Road, Honolulu, Hawaii 96822, USA*
[6]*GSECARS, University of Chicago, 9700 S Cass Ave, Argonne, Illinois 60439, USA*
[7]*Department of Physics and Astronomy, University of Tennessee, Knoxville, Tennessee 37996, USA*
[8]*Materials Science and Technology Division, Oak Ridge National Laboratory, Oak Ridge, Tennessee 37831, USA*

(Received 20 November 2022; revised 31 March 2023; accepted 31 March 2023; published 13 April 2023)

We have studied the insulator-to-metal transition and crystal structure evolution under high pressure in the van der Waals compound $CoPS_3$ through *in situ* electrical resistance, Hall resistance, magnetoresistance, x-ray diffraction, and Raman scattering measurements. $CoPS_3$ exhibits a $C2/m \rightarrow P\bar{3}$ structural transformation at 7 GPa accompanied by a 2.9% reduction in the volume per formula unit. Concomitantly, the electrical resistance decreases significantly and $CoPS_3$ becomes metallic. This metallic $CoPS_3$ is a hole-dominant conductor with multiple conduction bands. The linear magnetoresistance and the small volume collapse at the metallization suggest the incomplete high-spin → low-spin transition in the metallic phase. Thus, the metallic $CoPS_3$ possibly possesses an inhomogeneous magnetic moment distribution and short-range magnetic ordering. This paper summarizes the comprehensive phase diagram of MPS_3 (M = V, Mn, Fe, Co, Ni, and Cd) that metalize under pressures.

DOI: 10.1103/PhysRevB.107.165125

I. INTRODUCTION

The transition-metal thiophosphate MPS_3 (M = V, Mn, Fe, Co, Ni, and Cd) compounds form a family of quasi-two-dimensional (2D) compounds. They are isostructural in a monoclinic $C2/m$ symmetry, with individual lamellae composed of slightly distorted octahedral sites circumscribed by the S atoms bordering the van der Waals gap which are, in turn, arranged in a honeycomb lattice. Of the octahedra, 2/3 can be described as a +2 metal cation in an MS_6 cage. The remaining 1/3 of the octahedra are filled with P-P dimers that form a $[P_2S_6]^4-$ anionic sublattice that charge balances the aforementioned metal cations. The anionic sublattice is common to all of these compounds; the cations, in turn, impart the various functionalities native to these systems, including magnetism [1,2]. In this particular subset of the metal thiophosphate family, many compounds form a Mott insulating state at low temperatures and exhibit 2D antiferromagnetic (AFM) behavior, except for the Cd and Zn, where the +2 oxidation state of the metal cation yields a closed d shell [3–7]. The 2D magnetism in these materials has attracted recent attention due to the ability to study the effects of extreme anisotropy in low dimensions. The MPS_3 family thus offers a convenient materials platform to study magnetic phenomena in low-dimensional materials in addition to the promise for applications in magnetic and spintronic devices because they can be exfoliated down to thin films [8–11]. Therefore, elucidating these interesting 2D magnetic materials' physical properties is vital for future applications. In particular, it is essential to consider the structural and magnetic changes induced by imparting pressure to these materials.

External pressure is an effective perturbation tool because van der Waals compounds are highly compressible, especially in the interlayer direction. Thus far, the structural, magnetic, and electronic evolutions under compression have been extensively studied for the MPS_3 (M = V, Mn, Fe, Ni, Cd) and their analogous selenophosphate counterparts $MPSe_3$. Researchers have commonly observed that these materials exhibit an insulator-to-metal transition at high pressures (12–28 GPa) [7,12–18]. Additionally, spin-crossover (high to low-spin state) occurs in $FePS_3$ ($FePSe_3$) and $MnPS_3$ ($MnPSe_3$) concomitantly with the insulator-to-metal transition [13,14]. Finally, $FePSe_3$ becomes superconducting with a superconducting transition temperature of 2.5 K at 9 GPa (increasing to 5.5 K at 30 GPa) [14]. Evidence for a metallization has also been reported recently in a bimetallic metal thiophosphate, Cu-deficient $CuInP_2S_6$ [19]. External pressure induces interlayer sliding transitions, followed by a 10–20% volume collapse across the insulator-to-metal transition at room temperature [4,12,13,15,17,18,20,21]. Other transitions can be more subtle. For example, the MPS_3 (M = Fe, Mn) and $V_{0.9}PS_3$ compounds change from $C2/m$ to a $C2/m$

*tmatsuok@utk.edu
†dmandrus@utk.edu

with a different monoclinic angle (β) or a trigonal $P\bar{3}1m$ [4,12–14,18,21–24]. $CdPS_3$ changes from $C2/m$ to a trigonal $R\bar{3}$ [20]. Previous studies of $NiPS_3$ observed up to five high-pressure phases ($P\bar{3}$, $P\bar{3}m1$, $P3m1$, $P3$, and $P1$) between ambient pressure and 39 GPa, making this composition unique among these van der Waals gapped magnetic materials [25]. Clearly, pressure-driven structural phase transitions are critical as drivers of unique states of matter with the potential to host emergent properties.

Focusing on the last of these properties, the trigonal distortion present in the octahedra bounding the metal cations (where the trigonal axis is parallel to the stacking direction) affects the degeneracy of the energy states associated with the octahedral crystal field splitting, thus creating highly anisotropic effects in the magnetism of these compounds [1] that, in turn, contribute to their interesting behavior. From a structural perspective, the magnetic MPS_3 or $MPSe_3$ can be grouped into three main categories. In all compounds, spins are pointed along the c axis except for $NiPS_3$ and $CoPS_3$, where spins are pointed parallel and antiparallel to the a direction.

The first grouping is $MnPS_3$ and $MnPSe_3$; both of these compounds are colinear antiferromagnets with propagation vectors of $\boldsymbol{q} = [0\ 0\ 0]$ [26–28]. We note that other works state that $\boldsymbol{q} = [0\ 1\ 0]$ for $MnPS_3$ [5]. The second main grouping contains $CoPS_3$ and $NiPS_3$; they exhibit $\boldsymbol{q} = [0\ 1\ 0]$ [3,6]. In $CoPS_3$, though the orientation of the moments is mostly along the a axis, a small component may be along the c axis as well [3]. Finally, the third grouping comprises the compounds $FePS_3$ and $FePSe_3$. The sulfide has been shown to have an incommensurate $\boldsymbol{q} = [1/2\ 1/2\ 0.34]$ [29] while the selenide has a vector of $\boldsymbol{q} = [1/2\ 0\ 1/2]$ [27,28]. The careful reader may note that $V_{0.8}PS_3$ [30], $NiPSe_3$ [31], and many of the quarternary magnetic compounds [1] have yet to be fully characterized in terms of magnetic structure and may yield fruitful investigations themselves if suitably sized crystals can be synthesized.

To date, the effects of high pressure on $CoPS_3$ have not been experimentally reported, probably due to the significant difficulty in the synthesis and single crystal growth of this compound. $CoPS_3$ is AFM at ambient pressure with a Neel temperature of $T_N = 122$ K and a Weiss temperature of $\theta = -116$ K [32]. Its effective moment is 4.9 μ_B, slightly larger than the expected value for a pure spin moment of a Co^{2+} ($S = \frac{3}{2}$) cation [32], implying some degree of orbital contribution to the magnetization. A first-principles calculation from an article dedicated to the pressure effects in $CoPS_3$ predicts a pressure-driven isostructural Mott transition accompanied by a spin crossover [33].

In this paper, we successfully grew large single crystals of $CoPS_3$. Our electrical resistance, Raman scattering, and x-ray diffraction (XRD) measurements reveal an insulator-to-metal transition around 7 GPa, coinciding with a $C2/m \rightarrow P\bar{3}$ structural transformation and a 2.9% reduction in the volume per formula unit. Hall effect measurements find the metallic phase is a hole-dominant conductor. The linear magnetic field dependence of the magnetoresistance (MR), combined with the small volume collapse at the metallization, suggests an incomplete high-spin $\rightarrow$ low-spin crossover in the metallic phase. Thus, metallic $CoPS_3$ may possess an inhomogeneous magnetic moment distribution and short-range magnetic ordering due to the coexisting high- and low-spin Co^{2+} ions. This paper summarizes the comprehensive phase diagram of MPS_3 that metalizes under compression.

II. EXPERIMENTAL METHOD

We synthesized single crystals of $CoPS_3$ using the general procedures outlined in Refs. [1,3]. Co powder (Alfa Aesar Puratronic, 22 mesh, 99.998%, reduced), P chunks (Alfa Aesar Puratronic, 99.999%), and S (Alfa Aesar Puratronic, 99.9995%) were combined in a near-stoichiometric ratio to form $CoPS_3$ together with an appropriate quantity of I_2 as the vapor transport agent in a sealed quartz ampoule, heated to the reaction temperature, and held there for four days [34]. Typical crystals were 4–6 mm in size along the a-b planes with several exceeding 12 mm. Typical thicknesses were $<$ 0.5 mm.

We used diamond anvil cells (DACs) for the high-pressure application. We loaded a small single crystal of $CoPS_3$ in a DAC and connected five electrical probes made of platinum (Pt) for the electrical resistance, MR, and Hall resistance measurements. The a-b planes of the single crystals were laid on the diamonds flat surface to achieve a quasiuniaxial compression. A precompressed sodium chloride (NaCl) flake was placed underneath the sample, serving as a pressure-transmitting medium and ensuring that the pressure distribution across the sample was as homogeneous as possible. Several tiny ruby chips (Cr: Al_2O_3) were added with the samples as a pressure standard [35]. For further details, see the Supplemental Materials [36].

We performed Raman spectroscopy measurements on a $CoPS_3$ crystal compressed in a DAC using a Renishaw inVia Raman microscope with a 632.8 nm excitation laser at room temperature. The pressure-transmitting medium was a 4:1 ratio methanol/ethanol solution. The power of the excitation laser was tuned to $\sim$1 μW to minimize heating.

We conducted the XRD measurements at beamline 13BM-C at the Advanced Photon Source (APS), Argonne National Laboratory, utilizing a focused [12 μm (H) $\times$ 18 μm (V)] x-ray beam (wavelength = 0.4340 Å) in all measurements. Potassium chloride (KCl) was the pressure-transmitting medium. We collected diffraction data on a flat panel detector array (Dectris Pilatus 1M-F, pixel size: 172 $\times$ 172 μm^2) in the forward scattering geometry at room temperature. We used Dioptas for two-dimensional XRD data reduction [37]. We obtained lattice constants (a, b, and c) by the least-square-fitting of peak positions using PDindexer [38].

III. RESULTS

A. Resistance versus pressure and temperature

Figure 1(a) shows the pressure dependence of the electrical resistance (R_{xx}) of $CoPS_3$ at room temperature without applying an external magnetic field. To estimate the figure of electrical resistivity (ρ_{xx}), we calculated ρ_{xx} for sample No. 1 using the area/length ratio wt/l where $w = 55$ μm is the width of the sample, $t = 20$ μm is the thickness, and $l = 50$ μm is the separation between electrical leads measured

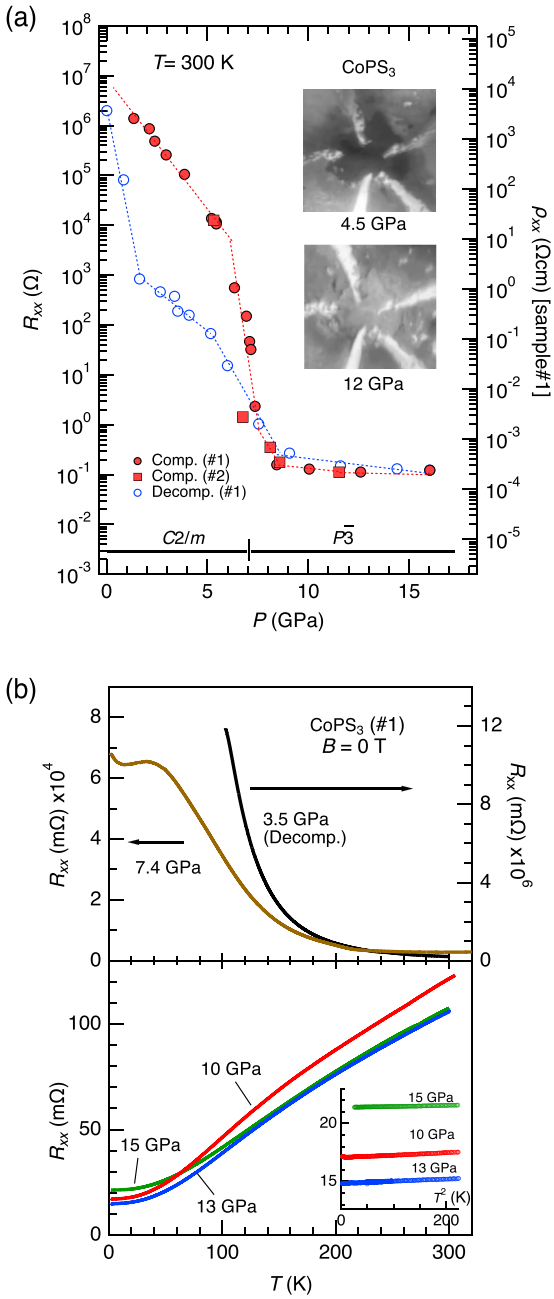

FIG. 1. (a) R_{xx} and ρ_{xx} versus P at room temperature. The data of samples No. 1 and No. 2 are plotted for compression and decompression. The dotted lines are guides for the eyes. The vertical and horizontal solid lines indicate the structural phase diagram confirmed by our XRD and Raman scattering measurements. The inset pictures show sample No. 1 at pressures. (b) R_{xx} versus T at pressures obtained for Sample No. 1 without an external magnetic field. All data plots are taken on warming. The inset figure plots the R_{xx} versus T^2.

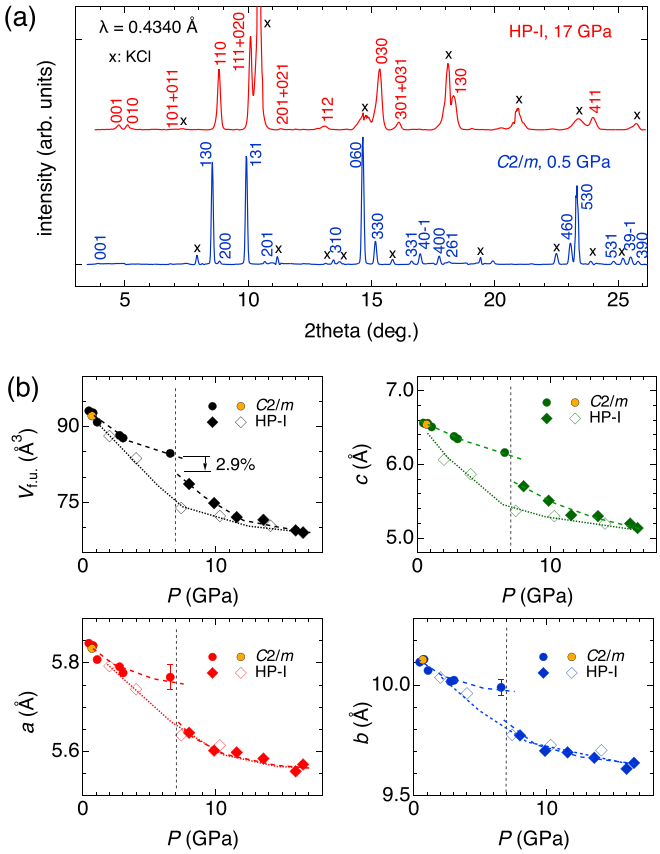

FIG. 2. Structure analysis of $CoPS_3$ by XRD under pressure. (a) XRD patterns of the $C2/m$ (0.5 GPa) and HP-I (17 GPa) phases. Note that KCl changes from B1- to B2-type structure at 2 GPa. (b) Pressure evolution of $V_{\text{f.u.}}$ and lattice constants. The trigonal structure of HP-I is reduced to a monoclinic lattice ($\beta = 90^\circ$) for comparison. The open and closed data points indicate compression and decompression, respectively. The error bars are inside the data markers at most pressures except for 6.8 GPa. The broken and dashed curves are guides for the eyes. The vertical dotted line is the structural phase boundary.

before applying pressure. Since the separation between electrical leads does not change significantly [Fig. 1(a)], we assume that most of the change in ρ_{xx} comes from the reduction of t. From the XRD results [Fig. 2(b)] discussed later, the c axis shrinks 20% from the ambient pressure to the highest pressure (17 GPa). Although the error does not affect the conclusion of the current paper, readers should note that a maximum of 20% error should be included in the ρ_{xx} in Fig. 1(a). We also note that we obtained the pressure by averaging the pressure values measured at room temperature before and after each temperature cycle for the electrical resistance measurements. The actual pressures at low temperatures are thought to be somewhat different from the indicated values.

The R_{xx} decreases into the measurable range of our transport measurement system (maximum 2 MΩ) above 2 GPa. The R_{xx} shows a significant decrease up to 7 GPa by three orders of magnitude. Then, it abruptly decreases by five further orders of magnitude when applying an additional mere 1 GPa. Above 10 GPa, R_{xx} becomes almost independent of the external pressure. The ρ_{xx} reaches ∼200 $\mu\Omega$cm, suggesting a metallic conductivity. The similarities in the trends from two independent samples, No. 1 and No. 2, show good reproducibility of the transport results [Fig. 1(a)]. The insets of Fig. 1(a) show microphotographs of $CoPS_3$ at 4.5 GPa and 12 GPa under epi-illumination. Here we see that the light reflection increases with pressure. The sample at 12 GPa is

shiny and comparable to the Pt metal of the electrical probes, thus indicating a major electronic transition.

Upon releasing the pressure, the R_{xx} traces back the R_{xx} versus P curve of the compression down to 8 GPa. Below 8 GPa, the R_{xx} stays much lower (one to three orders of magnitude) than the compression, showing a large hysteresis. However, at 0 GPa, the compressed and decompressed lines are extrapolated to merge. This large hysteresis between compression and decompression implies the presence of a first-order transition.

To see if there are any temperature-dependent resistance effects, in Fig. 1(b) (top panel), we show R_{xx} versus T at various pressures (sample No. 1) without an external magnetic field. The $CoPS_3$ exhibits insulating or semiconducting behavior at 7.4 GPa and also displays a negative slope (dR_{xx}/dT). The origin of the hump at 7.4 GPa and 50 K is as of yet unknown. Above 10 GPa, dR_{xx}/dT becomes positive along the entirety of the probed temperature range, thus revealing that $CoPS_3$ is metallic under these pressures. We see no superconducting transition down to 2 K. When we plot the R as a function of T^2 [inset in the bottom panel of Fig. 1(b)], we see that dR_{xx}/dT fits the Fermi-liquid theory at temperatures below 15 K. Thus, we conclude that $CoPS_3$ exhibits a pressure-induced insulator-to-metal transition around 7 GPa. At 3.5 GPa on decompression, $CoPS_3$ exhibits an insulator behavior [Fig. 1(b)].

B. XRD

Figure 2(a) displays the representative XRD patterns of $CoPS_3$ at 0.5 and 17 GPa. We note that the observed XRD patterns are affected by the orientation reflecting the initial geometry of the single crystal when loaded in the DAC. In our measurements, the *a*-*b* plane of the layered structure is perpendicular to the x-ray beam. Although we rotated the DAC as much as allowed by the beamline instruments and the DAC opening angle, the diffraction peaks from (hkl) with large l (>2) are invisible, limiting the number of peaks. Additionally, the single crystal partially broke into several pieces during compression. Therefore, the relative intensity between the diffraction peaks is inaccurate because the obtained XRD results are not in the form of even-intensity powder rings. See the Supplemental Material for the XRD image recorded on a detector [36]. At 0.5 GPa, the XRD peak positions agree well with the previously reported monoclinic $C2/m$ [$a = 5.844(1)$ Å, $b = 10.127(1)$ Å, $c = 6.562(4)$ Å, $\beta = 107.04(2)^\circ$] [3]. At 17 GPa, we can index the XRD pattern to a trigonal structure with lattice constants $a = b = 5.570(5)$ Å, $c = 5.13(2)$ Å. We name the high-pressure trigonal phase HP-I in this paper.

Figure 2(b) shows the pressure dependencies of volume per formula unit ($V_{\text{f.u.}}$) and the lattice constants a, b, and c. The $V_{\text{f.u.}}$ is obtained by dividing a unit cell volume by the number of $CoPS_3$ units. For the comparison between $C2/m$ and HP-I, we reduced the trigonal unit cell to a monoclinic unit cell ($\beta = 90^\circ$) using the relation $b_{\text{mono}} = 2a_{\text{tri}} \times \cos 30^\circ$. In agreement with the electrical transport measurements, the structure changes from $C2/m$ to HP-I at 7 GPa. Concomitantly, the $V_{\text{f.u.}}$ abruptly decreases by 2.9% (84.690 Å^3 → 82.269 Å^3) at 7 GPa. All the lattice constants a, b, and c show sharp discontinuities, with c exhibiting the largest reduction ($\Delta c = 1.4$ Å).

Here, we focus on the observed reduction in the $V_{\text{f.u.}}$. Isostructural materials $MnPS_3$ and $FePS_3$ commonly collapse a volume by 10–20% simultaneously with a spin crossover, and the insulator-to-metal transition [13–15]. This study has not performed a direct measurement, such as x-ray absorption and Mössbauer spectroscopy, to investigate the electronic configuration of Co. However, from the observed volume collapse and comparing $FePS_3$ and $MnPS_3$, it is reasonable to conclude that $CoPS_3$ exhibits the spin crossover ($S = 3/2 \rightarrow 1/2$) accompanied by the metallization at 7 GPa.

On the other hand, the observed volume reduction (2.9%) of $CoPS_3$ is much smaller than $MnPS_3$ (19.7%) and $FePS_3$ (10.6%) [13–15]. The ionic radii of high- (HS, 0.89 Å) and low-spin (LS, 0.79 Å) Co^{2+} ions [39] make the HS → LS radius reduction 11.2%, which is not much smaller than that of Mn^{2+} (HS: 0.97 Å, LS: 0.81 Å, 16.5%) and Fe^{2+} (HS: 0.92 Å, LS: 0.75 Å, 18.5%) [39]. Thus, the slight volume reduction of $CoSP_3$ cannot be explained simply by the difference between HS and LS radii.

In Fig. 2(b), it is also noticeable that the $V_{\text{f.u.}}$ and c in the HP-I phase show a steeper compression between 7 GPa and 12 GPa followed by moderate compression above 12 GPa, indicating a sign of $V(P)$ stabilization. These series of changes in compressive behavior suggest an electronic transition takes place in the HP-I phase. On decompression, the HP-I phase remains down to 2 GPa, revealing a large hysteresis in $V_{\text{f.u.}}$ and c below 12 GPa. Considering the significant hysteresis observed in R_{xx} versus P, the $C2/m$ →HP-I transition is considered first order. We later discuss these anomalous compressions concerning electronic transformations, the HS to LS crossover, and the volume collapse.

C. Raman scattering

To obtain further insights into changes to the symmetry of the crystal structure under compression, we performed pressure-dependent Raman scattering measurements. Figure 4(a) displays the evolution of the Raman spectra from $CoPS_3$ under quasihydrostatic compression at room temperature. Based on previous theoretical and experimental reports, we anticipate eight Raman active modes ($5E_g + 3A_g$) for bulk $CoPS_3$ at room temperature [40]. At pressures below 6.7 GPa (in the stability region of $C2/m$), we observe all eight peaks in agreement with the previous reports [40]. The peak at 110 cm^{-1} is not observed at atmospheric pressure but becomes visible above 1.2 GPa, suggesting that a preferential alignment of layers could cause this peak to be more prominent at higher pressures. Up to 6.7 GPa, all the peaks blueshift in frequency with increasing pressure, as expected for phonon modes under compression. Between 6.7 GPa and 7.5 GPa, the Raman spectrum changes abruptly with the loss of peaks and the appearance of new peaks [Figs. 3(a) and 3(b)]. Accompanied by the Raman spectral change, the sample becomes lighter in color and more reflective under epi-illumination [Fig. 3(a), photographs], in agreement with the visible observations during our transport measurements [Fig. 1(a)]. The abrupt Raman spectra and reflectivity changes give further evidence of the $C2/m$ →HP-I structural change

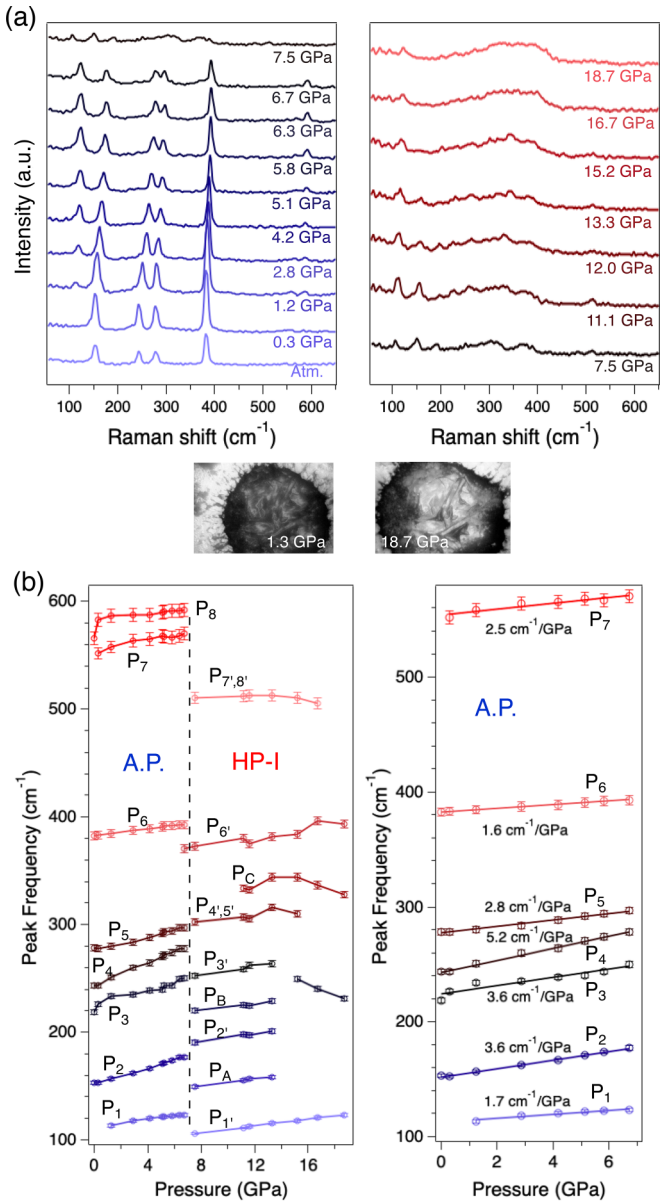

FIG. 3. Raman scattering measurements of $CoPS_3$ under pressures. (a) The pressure evolution of the Raman scattering spectra at ambient temperature. Pictures show $CoPS_3$ at 1.3 GPa and 18.7 GPa. Atm.; atmospheric pressure [(b), left]. Pressure dependencies of the Raman scattering peaks. Dashed vertical lines show the structural phase boundaries. (b), right: The close-up view of the left panel. See the Supplemental Materials for the peak-fitting analysis [36].

coinciding with the ITM transition. Similar to what our electrical resistance measurements observe, the transition in the Raman spectra takes place within a narrow pressure range of 0.8 GPa, strongly suggesting the absence of an intermediate phase between $C2/m$ and HP-I phases. At 18.7 GPa, all peaks diminish significantly and are replaced by a broad peak between 300–400 cm^{-1}, except for the peak near 120 cm^{-1}. We consider two possibilities for the cause of broadening. One is the solidification of the pressure-transmitting medium near 10 GPa, and the developing nonhydrostatic condition that induces the inhomogeneous strain in the crystal [41–43]. Another possibility could be the indication of further structural transformation. Future studies would address the question.

Figure 3(b), left panel, shows the pressure-dependent frequencies of the Raman peaks. The right panel in Fig. 3(b) shows a magnified view of the ambient pressure phase. Based on the previous literature, we assign the peak P_4 near 245 cm^{-1} to the out-of-plane bending (A_{1g}) of $P_2S_6^{4-}$ dimer units. It has the highest pressure coefficient, reflecting the large compressibility in the c axis [Fig. 3(b)] [40]. P_8 near 560 cm^{-1} is the out-of-plane stretching of the P-P dimer (E_g) [40]. The peak shows a sharp increase in the frequency at the start of compression. On the contrary, P_6 near 380 cm^{-1}, representing in-plane stretching of $P_2S_6^{4-}$ units (A_{1g}) has the lowest pressure coefficient [40]. Overall, the compression affects out-of-plane phonon modes more than in-plane modes.

Next, we try to understand the $C2/m \rightarrow$ HP-I transition. We first track the peak frequency changes across the structural transition. P_1 near 115 cm^{-1} (complex vibrations along all three axes of Co and S, E_g) blue shifts with pressure up to 7 GPa, above which it redshifts in frequency [labeled $P_{1'}$ in Fig. 3(b)]. P_2 near 145 cm^{-1} (in-plane Co-Co stretching, E_g) and P_3 near 238 cm^{-1} (out-of-plane stretching of $P_2S_6^{4-}$, E_g) behave similarly to P_1, blueshifting up to 7 GPa, followed by slight discontinuities and are designated as $P_{2'}$ and $P_{3'}$in the HP-I phase, respectively. P_4 near 240 cm^{-1}merges with P_5 near 280 cm^{-1} (in-plane S-S vibration in $P_2S_6^{4-}$ units, E_g) up to 7 GPa. In the HP-I phase, the merged peak is designated $P_{4',5'}$ near 300 cm^{-1}. P_6 near 380 cm^{-1} (in-plane S-S vibration, A_{1g}) exhibits a sharp discontinuity across the phase transition and appears at a lower frequency 400 cm^{-1} labeled as $P_{6'}$. P_7 near 545 cm^{-1} (complex stretching mode of $P_2S_6^{4-}$, E_g) and P_8 come closer up to 7 GPa. Across the critical pressure, these peaks disappear, and the highest frequency peak in HP-I appears at a much lower frequency 510 cm^{-1}, designated as $P_{7',8'}$. The merging and newly appearing peaks provide evidence for both increasing and decreasing symmetry.

We next consider the evidence for increased symmetry. As mentioned above, several Raman peaks merge with increasing pressure up to 7 GPa ($P_4 + P_5 \rightarrow P_{4',5'}$ and $P_7 + P_8 \rightarrow P_{7',8'}$). This means that in addition to the mirror planes, axial glides, inversion centers, twofold rotations, and the twofold screw axes that characterize the $C2/m$ space group, the system gains additional symmetry elements across 7 GPa. Examination of the $C2/m$ group $\leftrightarrow$ supergroup relationships provides several higher symmetry candidates such as $P\bar{3}1m$, $P\bar{3}m1$, and $Cmmm$. Since our XRD result suggests a trigonal structure, we can exclude $Cmmm$. See the Supplemental Materials of Ref. [25] for the summarized subgroup/supergroup symmetry relations relevant to the MPS_3 compounds.

Next, we investigate the evidence for symmetry breaking. The newly emergent peak P_A (near 140 cm^{-1}) in the HP-I phase indicates the rise of the out-of-phase intralayer Co translational mode. P_B and P_C are considered to be related to the S-S vibrations from their frequencies in the lower-pressure phase. To unravel how these modes correspond to the change in crystal symmetry, we consider the relevant mode displacement patterns and how they impact different symmetry elements. These include some symmetry elements

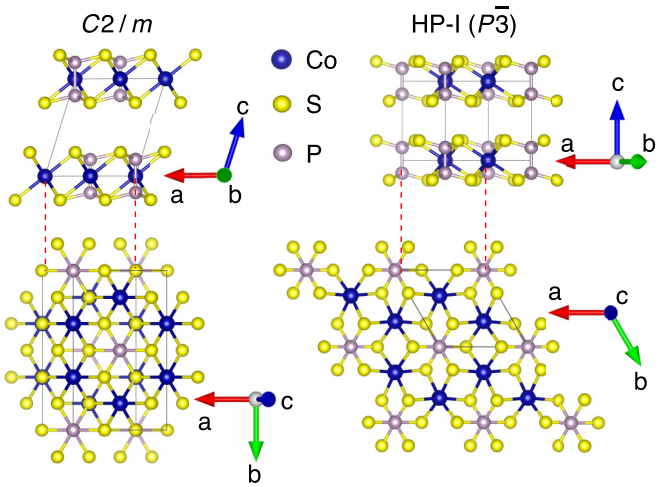

FIG. 4. The crystal structure of ambient pressure (A.P.) phase ($C2/m$) and the suggested $P\bar{3}$ structure for HP-I phase visualized using VESTA [44].

of $P\bar{3}1m$ and $P\bar{3}m1$, such as axial glide planes, twofold rotations, and twofold screw axes. Therefore, candidate subgroups include $P31m$, $P\bar{3}$, $P3m1$, and $P312$. In the Raman spectra, we do not see a significant increase in the overall number of peaks, suggesting the retention of the inversion center. Of the four candidate subgroups, $P\bar{3}$ retains the inversion center. We, therefore, conclude the $C2/m \rightarrow P\bar{3}$ transformation.

Figure 4 summarizes the crystal structures of $CoPS_3$ in the $C2/m$ and $P\bar{3}$. Note that we did not refine the atomic positions in the $P\bar{3}$ due to the limitation mentioned above in the obtained XRD data [36].

We calculated the mode Grüneisen parameter for each phonon mode using the pressure dependence of the Raman frequencies and the $V_{\text{f.u.}}$. See the Supplemental Materials for the analysis and results [36].

D. Transverse transport measurements

Now that we have confirmed the existence of a metallic phase at high pressure in $CoPS_3$, we turn our attention to its electronic properties. Transverse transport measurements, including Hall resistance and MR, are essential probes because it gives us information about the Fermi surface [45]. Figures 5(a) and 5(b) display the Hall resistivity (ρ_{xy}) and MR [$\Delta\rho_{xx}(B)/\rho_{xx}(0)$] of sample No. 1 at 10, 13, and 15 GPa and temperatures ranging from 1.8 to 160 K. The ρ_{xy} shows positive and mostly linear magnetic field dependence at all temperatures and pressures [Fig. 5(a)]. In addition, it does not saturate at this study's highest field (9 T). If a material is ferromagnetic, the anomalous Hall effect is anticipated with saturation at a high field. Our Hall resistance data thus indicate that $CoPS_3$ is not ferromagnetic. $CoPS_3$ is likely a hole-dominant conductor that requires a multiple-conduction band model. We also note that $\Delta\rho_{xx}(B)/\rho_{xx}(0)$ exhibits a positive and linear magnetic field dependence [linear magnetoresistance (LMR)] at all pressures and temperatures [Fig. 5(b)].

Generally, a multiband analysis based on a semiclassical description utilizes information such as carrier density and mobility on the Fermi surface from the Hall resistivity and MR. However, the obtained results tend to become ambiguous because of hypothesizing the number of carrier types. The LMR in this study makes the analysis even more complicated because it is far from the quadratic behavior anticipated by a semiclassical description. Here we employ a simple one-band model analysis and estimate the orders of density ($n_{e,\text{av}}$) and mobility ($\mu_{e,\text{av.}}$), on average, for all carriers. From the relation $1/eR_H = n_{e,\text{av}}$, the Hall coefficient (R_H) and the electron charge (e) provide the estimation $n_{e,\text{av}} = 1.41 \times 10^{21}$ cm^{-3} at 10 GPa and 1.8 K. This value is slightly smaller than that a Hall effect measurement expects for general metals (10^{22} cm^{-3}). Using the relation $\sigma = \mu_{e,\text{av}} n_{e,\text{av}}$, the $\mu_{e,\text{av}} = 138$ cm^{2}V^{-1}s^{-1} can be extracted, where σ is a conductivity. The $n_{e,\text{av}}$ and $\mu_{e,\text{av}}$ are within the range of 1.4–2.9 $\times 10^{21}$ cm^{-3} and 55–138 cm^{2}V^{-1}s^{-1} at 2 K for all pressures, respectively.

Here, we analyze the observed LMR [Figs. 5(b) and 5(c)]. The semiclassical model predicts that the ρ_{xx} evolves quadratically with a magnetic field, saturating at high fields if the hole and electron densities are not compensated [46,47]. At the low-field limit, $\omega_c\tau \ll 2\pi$, where ω_c is the cyclotron frequency and τ is the relaxation time, the leading term in ρ_{xx} becomes $\Delta\rho = \rho(B) - \rho(B = 0) \sim H^2$ due to Onsager reciprocity relation, which requires $\sigma_{ij}(\boldsymbol{B}) = \sigma_{ji}(-\mathbf{B})$ [46,47]. The ρ_{xx} of $CoPS_3$ evolves almost linearly with the field contrary to the semiclassical description. The LMR is observable down to low fields: 0.7 T at 10 GPa, 2 T at 13 GPa, and 3 T at 15 GPa [Fig. 5(c)] followed by the asymptotic curves approaching zero near zero field. Elevated temperature suppresses the increase of the ρ_{xx} versus B curves. At higher pressures, the parabolic shape in the ρ_{xx} versus B becomes more evident at lower fields. To obtain further insight into the linear term in the ρ_{xx} versus B relation, we adopt a phenomenological approach to disentangle these components, fitting the measured MR as $\rho_{xx}(H, \text{various } T) = \rho_{xx}(T, H = 0) + A(T)H + B(T)H^2$ [48]. We perform the fitting below 4 T where the quadratic component is visible. Figure 5(d) plots $A(T)$ and $B(T)$ as a function of temperature. The $A(T)$ saturates below 10 K, significantly decreasing with increasing temperature. At low temperatures, the $A(T)$ decreases with pressure from 10 to 13 GPa. However, the change becomes diminished between 13 and 15 GPa. By comparison, the $B(T)$ does not change appreciably over a wide range of temperatures. We try to discern the origin of LMR in the following section.

IV. DISCUSSION

Here we discuss the electronic configuration of the metallic $CoPS_3$, discerning the source of the observed pressure dependencies of $V_{\text{f.u.}}$ and the LMR. First, we focus on the $V_{\text{f.u.}}$ reduction at $C2/m \rightarrow P\bar{3}$ transformation. As discussed earlier, we concluded HS $\rightarrow$ LS spin crossover takes place at the insulator-to-metal transition and structural transformation. However, the relatively small reduction in the $V_{\text{f.u.}}$ is not explained simply by the decrease in the ionic radius of Co^{2+}. Remarkably, a recent theoretical study predicts that the magnetic moment in $CoPS_3$ is much more robust than Fe^{2+} and Mn^{2+} under pressure [33]. This same study suggests that the $CoPS_3$ in either the $R\bar{3}$ or $C2/m$ ($\beta \sim 90^\circ$) phases above 12.5 GPa is ferromagnetic. The magnetic moments of Co^{2+} decrease significantly with increasing pressure but do not achieve $S =$

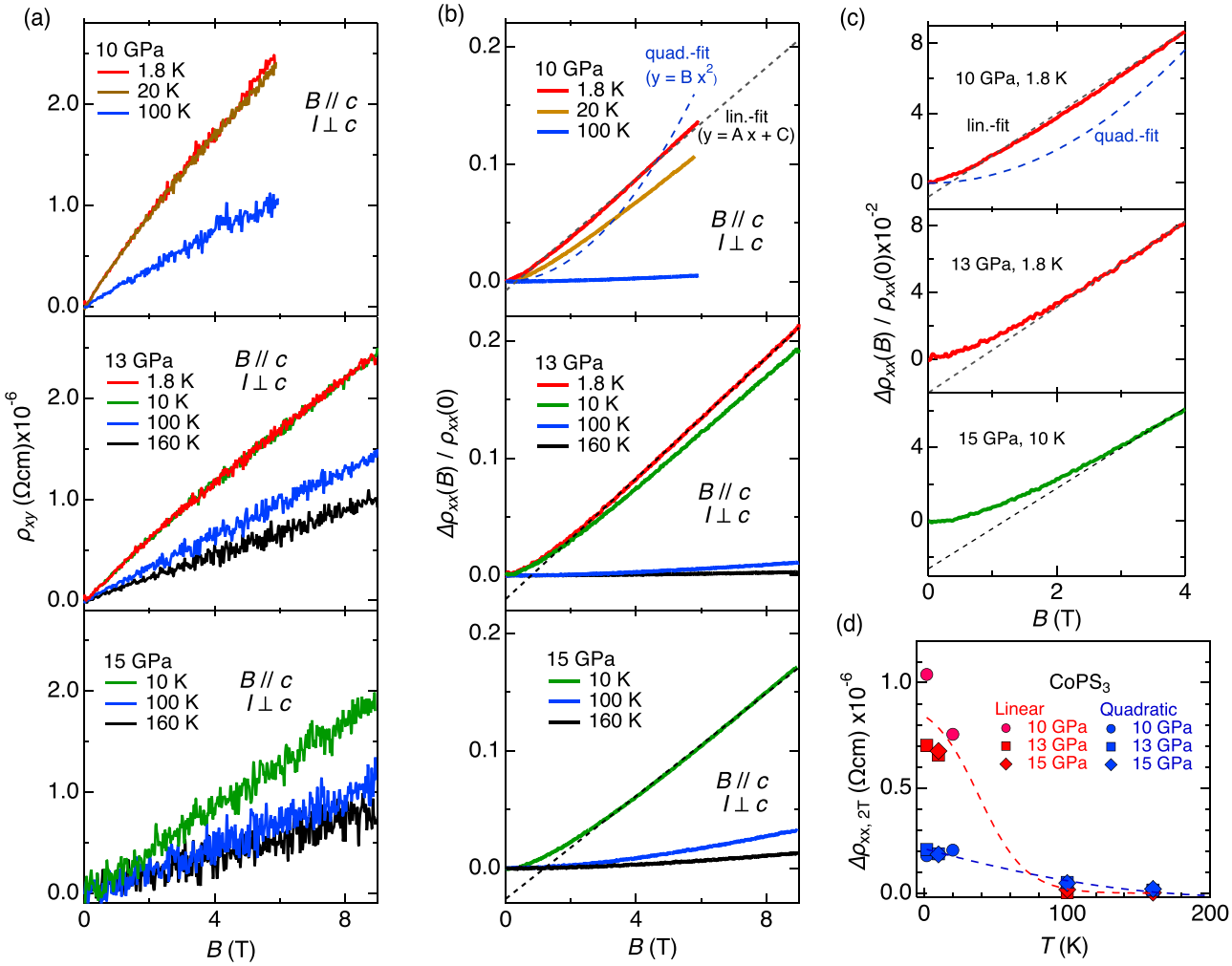

FIG. 5. Transverse transport data from metallic $CoPS_3$ at 10, 13, and 15 GPa. (a) The ρ_{xy} at different temperatures. The data at 1.8 K and 20 K at 10 GPa overlap (top panel). The data at 1.8 K and 10 K at 13 GPa overlap (middle panel). (b) The $\Delta\rho_{xx}(B)/\rho_{xx}(B=0)$. The dotted (black) and dashed (blue) lines in the top panel indicate the linear fit, $y = Ax + C$ with $A = 1.927(3)\times10^{-3}$, $C = -7.7772(3) \times 10^{-3}$) and quadratic fits [quad. fit, $y = Bx^2$ with $B = 4.82(4) \times 10^{-3}$] to the data at 10 GPa and 1.8 K. (c) $\Delta\rho_{xx}(B)/\rho_{xx}(B=0)$ at low field. (d) The linear and quadratic components of MR under a field of 4 T for $CoPS_3$. The broken lines are a guide for eyes.

1/2 even at 50 GPa [33]. Although the predicted crystal structure differs from the one our experiments determine, we thus raise the possibility that the $P\bar{3}$ phase is in the middle of spin crossover where the HS- and LS-Co^{2+} coexist.

We turn our eyes to the pressure dependencies of the $V_{\text{f.u.}}$ in the $P\bar{3}$ phase. Looking at several Fe-bearing compounds and (Mg, Fe)O forsterite, we find the changes in the pressure dependencies of the volume due to the interplay between the compressibility and spin variation effect on the Fe^{3+} ionic radii [49–51]. Considering the incomplete spin crossover discussed above, the significant reduction of $V_{\text{f.u.}}$ between 7 and 12 GPa is potentially due to the proceeding HS → LS crossover. Then, the moderate $V_{\text{f.u.}}$ versus P slope above 12 GPa suggests the spin crossover's completion or moderate progress. The significant hysteresis between the $V_{\text{f.u.}}$ of $P\bar{3}$ upon compression and decompression, especially below 12 GPa, could be because the sample on compression has a bigger fraction of HS than on decompression.

Next, we try to discern the source responsible for LMR. LMR has been observed in a growing number of materials and is often invoked as evidence for some exotic quasiparticles in these compounds [48,52–67]. At the high-field limit $\omega_c\tau \gg 2\pi$, where ω_c is the cyclotron frequency and τ is the relaxation time, there have been several suggested electronic and geometric mechanisms that satisfy the criteria for a quantum LMR. The first is special features on the Fermi surface, including the linear dispersion from a Dirac cone with infinitesimally small carrier mass [68–71]. The second is principally geometric in nature, including an average over a combination of open and closed electron trajectories in polycrystals [47,64,72–74].

On the other hand, the disorders of density and spin have been suggested as universal mechanisms. The density disorder provides an inhomogeneous distribution of charge concentration and affects the conduction carrier path, admixing the Hall resistance component with MR [67,69,74]. Similarly, the LMR due to the magnetic disorder has been observed for several 3*d* ferromagnets and the AFM normal conducting state of FeSe [75,76]. Another is the LMR in charge density wave (CDW) and spin density wave (SDW) containing materials

[48]. From their nature, those three are applicable to the LMR to low-field limit $\omega_c\tau \ll 2\pi$.

To examine the suggested mechanisms, we first estimate an average for all carriers $\omega_c\tau = B/\rho nec = 2.75 \times 10^{-2}$ at 2 T (10 GPa, 1.8 K) for $CoPS_3$. The criteria for quantum LMR ($\omega_c\tau \gg 2\pi$) (Ref. [69]) are thus not satisfied under our measurement conditions. Additionally, CDW and SDW are not likely, judging from the featureless ρ_{xx} versus T. Also, we do not observe the appearance of satellite peaks in XRD, which is suggestive of CDW. Finally, the rapid diminution of $A(T)$ [Fig. 5(d)] at elevated temperatures argues against the phonon- [70] or the excitation-based [66] scattering mechanisms.

We next test the density fluctuation scenario. Since our sample is under nonhydrostatic stress, it is the most straightforward one to consider. However, the estimated $n_{e,\mathrm{av}}$ and $\mu_{e,\mathrm{av}}$ are far bigger and smaller than that of the high-mobility and low-carrier density materials, respectively, where the density fluctuation effects become more prominent [67,74,77,78]. In addition, since the pressure gradient in the sample generally develops with pressure in a nonhydrostatic condition, a more amplified density fluctuation and even more linear MR are expected, contrary to our experimental results. Thus, we defer concluding the density fluctuations as the dominant source.

Finally, we consider the spin-disordered mechanism [75,76]. In this model, ions with different magnetic moments coexist randomly. The inhomogeneously distributed magnetic moments possibly affect the conduction carrier trajectories allowing irregular current paths and the LMR. Based on our conclusion of the incomplete HS $\rightarrow$ LS spin crossover, it can be thought that HS- and LS-Co^{2+} ions coexist and are arranged in a disordered manner, possibly possessing a short-range magnetic ordering. In Figs. 5(c) and 5(d), we see the quadratic component of the LMR becomes more evident in the ρ_{xx} versus B at higher pressure, implying a more homogeneous magnetic moment distribution promoted by pressure. In addition, the linear component at 13 GPa and 15 GPa possess almost the same value. Those observations are consistent with the interpretation that the spin crossover proceeds with pressure up to 12 GPa and stops or progresses moderately above 12 GPa in the $P\bar{3}$ phase.

The remaining question is how the insulator-to-metal transition, the structural transition, and the spin crossover relate to each other in $CoPS_3$. We propose two scenarios. The first is that the insulator-to-metal transition occurs simultaneously with the structural transition. The second is that metallization originates within the $P\bar{3}$ phase. This scenario arises from the observation that $CoPS_3$ is still a semiconductor at 7.4 GPa, while our Raman and XRD measurements suggest that the structural transformation occurs at 7 GPa and completes within 1 GPa. Besides, upon decompression, $CoPS_3$ reverts to an insulator at 3.5 GPa, preceding the $P\bar{3} \rightarrow C2/m$ transition observed below 2 GPa. Currently, we do not have precise and detailed data to address the discrepancy in the transition pressures. The off-stoichiometry of the sample may also affect the transition pressures. Future detailed studies including the simultaneous measurements of electrical

TABLE I. Structural and electronic phase diagram of MPS_3's that metalize under compression. AFM_{out} and AFM_{in} mean that the magnetic moments are pointing mostly in out-of-plane and in-plane directions, respectively. The P_c is the pressure where crystal structures start transformations. ΔV is the volume reduction at insulator-to-metal transition.

	A.P.	H.P.			Ref./Note
$V_{0.9}PS_3$	$C2/m$ ($\beta \sim 107°$)	$C2/m$ ($\beta \sim 90°$)			[12,22]
	AFM_{NA},[a] $\mathbf{q} = [010]$, ins.	ins.[b]	met.[c]		
P_c		2.6 GPa	12 GPa		
			$\Delta V \sim 0.8\%$		
$MnPS_3$	$C2/m$ ($\beta \sim 107°$)	$P\bar{3}1m$	$C2/m$ ($\beta \sim 90°$)		[13,18,23,24]
	AFM_{out}, $\mathbf{q} = [010]or[000]$, ins.	ins.	met.		spin crossover
P_c		10 GPa	28 GPa, $\Delta V \sim 19.7\%$		at 28 GPa
$FePS_3$	$C2/m$ ($\beta \sim 107°$)	$C2/m$ ($\beta \sim 90°$)	$P\bar{3}1m$		[4,14,21,23,24]
	AFM_{out}, $\mathbf{q} = [01\frac{1}{2}]$, ins.	AFM, $\mathbf{q} = [010]$, ins.	met.		spin crossover
P_c		2 GPa	14 GPa, $\Delta V \sim 10.6\%$		at 14 GPa
$CoPS_3$	$C2/m$ ($\beta \sim 107°$)	$P\bar{3}$			[3,23]
	AFM_{in}, $\mathbf{q} = [010]$, ins.	met.			this paper
P_c		7 GPa, $\Delta V \sim 2.9\%$			
$NiPS_3$	$C2/m$ ($\beta \sim 107°$)	$P\bar{3}$	$P\bar{3}1m$	$P3m1$	[16,17,23,25]
	AFM_{in}, $\mathbf{q} = [010]$, ins.	ins.	ins.	met.	
P_c		7.2 GPa	15 GPa	23 GPa	
				$\Delta V \sim 2.8\%$	
$CdPS_3$	$C2/m$ ($\beta \sim 107°$)	$R\bar{3}$	$R\bar{3}$		[20,23]
	ins.				
P_c	–	0.25 GPa	8.7 GPa		

[a]N.A.: information not available.
[b]ins.: insulator.
[c]met.: metal.

transport and crystal structure would provide an unambiguous answer.

Table I summarizes the structural and electronic evolution of MPS_3 (M = V, Mn, Fe, Co, Ni, Cd) reported to date. All MPS_3 exhibit $C2/m$ ($\beta \sim 107^\circ$) to trigonal structural transition when subjected to pressure, decreasing their monoclinic angle to 90° as a consequence of the interlayer sliding. The insulator-to-metal transition commonly occurs when MPS_3 compounds are in the trigonal or $C2/m$ with $\beta \sim 90^\circ$ symmetries.

The question is how the electronic configuration, magnetism, and structure correlate. We see that MPS_3 compounds, as far as the available experimental data display, can be classified into two groups concerning their pressure transformations. The first contains $MnPS_3$ and $FePS_3$ and exhibits the transformation between symmetries in the group-subgroup relation ($C2/m \leftrightarrow P\bar{3}1m$). These compounds align their magnetic moments mainly in the out-of-plane direction. The second group is comprised of $CoPS_3$ and $NiPS_3$. These materials have moments aligned largely in plane. Contrary to the first group, the transition process from the lower-pressure phase ($C2/m$) to the first high-pressure phase is not in the simple group-subgroup relation. As discussed, $CoPS_3$ transforms from $C2/m$ (14) to $P\bar{3}$ (147) via a higher-symmetry phase such as $P\bar{3}1m$ (162). $NiPS_3$ is an insulator in the $P\bar{3}$ phase. Thus, Ni^{2+} ions in the $P\bar{3}$ phase may possibly be in the HS state. The potentially remaining magnetic moments of Co^{2+}, and possibly Ni^{2+}, are likely to affect the high-pressure phase that succeeds the $C2/m$.

Figure 6 is the visual summary of the T_Ns and $V_{\text{f.u.}}$ shown in Table I as a function of the ionic radius of M in HS states. In Fig. 6, the two groups (Mn and Fe, Co and Ni) discussed for the pressure-induced structural transition are noticeable in the T_N and $V_{\text{f.u}}$. The $V_{\text{f.u.}}$s of $NiPS_3$ and $CoPS_3$ at 1 bar are similar. However, the $V_{\text{f.u.}}$ shows an obvious increase from $FePS_3$ to $MnPS_3$ while the ionic radius difference between Fe^{2+} and Mn^{2+} is smaller than between Ni^{2+} and Co^{2+}. The T_N decreases moderately with ionic radius from Ni^{2+} to Co^{2+}, followed by a steep decline from Fe^{2+} to Mn^{2+}. Remarkably, those two groups are also observable in the volume reduction from the insulator to the metallic phases at the metallization pressure. $NiPS_3$ and $CoPS_3$ commonly show a smaller reduction than another group (Fe and Mn). In MPS_3 compounds, the t_{2g} and e_g orbitals play roles in bonding, and the hopping integrals between t_{2g} and e_g show different anisotropies [7]. Thus, the occupation of the electron orbitals, partially filled t_2g and e_g orbitals of $FePS_3$ and filled t_{2g} in $NiPS_3$, for example, has a direct influence on the physical characteristics, making this group of compounds a rich platform to explore novel quantum phenomena. Figure 6 reveals that the electronic configurations at ambient pressure influence the high-pressure properties. We also notice that $MnPSe_3$ and $FePSe_3$ possess similar T_N with their analogous $MnPS_3$ and $FePS_3$. If Ni and Co follow this trend, we may expect T_Ns of $NiPSe_3$ and $CoPSe_3$ to be close to $NiPS_3$ and $CoPS_3$.

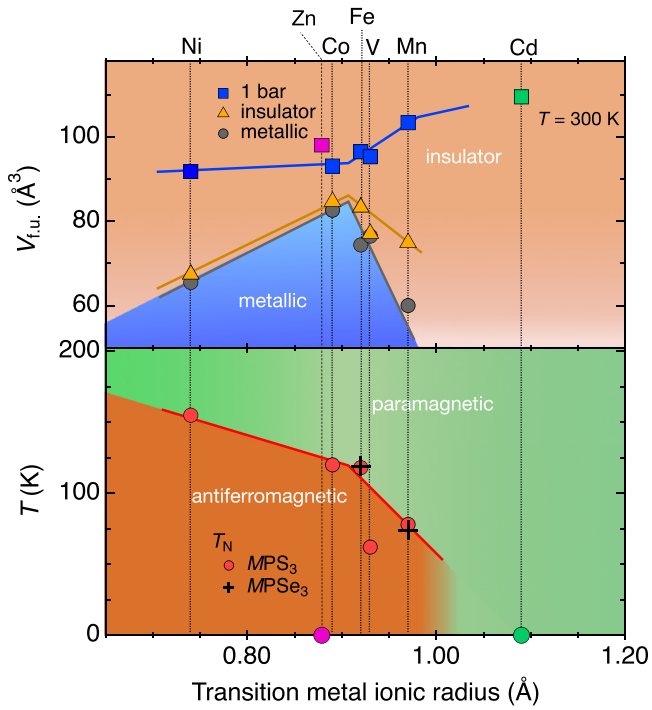

FIG. 6. MPS_3 phase diagram with temperature and volumes along the vertical axes and transition metal (M^{2+}) ionic radius in HS state (except for V) along the horizontal axis. Data are taken from Refs. [3,4,12–14,16–18,20,22–24,39,79]. The solid marks in the upper panel indicate the $V_{\text{f.u.}}$ at 1 bar (square), insulator phases (triangle), and metallic phases (circle). In the lower panel, the T_N of MPS_3 are plotted with $MnPSe_3$ and $FePSe_3$.

V. SUMMARY

We have successfully grown high-quality single crystals of $CoPS_3$ suitably large enough for conducting various high-pressure experiments. We studied the electrical transport and structural evolution of $CoPS_3$ under quasiuniaxial pressure along the layer-stacking direction through electrical resistance, Hall resistance, MR, Raman scattering, and XRD measurements. Electrical resistance significantly decreases as the pressure increases, consistent with the rise of the optical reflectivity of the sample. $CoPS_3$ becomes metallic above 7 GPa, accompanied by the monoclinic $C2/m \rightarrow$trigonal $P\bar{3}$ structural transition. Metallic $CoPS_3$ shows no superconducting transition down to 2 K. The $C2/m \rightarrow P\bar{3}$ transformation induces a 2.9% reduction in $V_{\text{f.u.}}$, much smaller than that of the Mn and Fe analogous. We analyzed the pressure-dependent phonon modes including the mode Gruneisen parameter [36,80]. The Hall effect data indicate the metallic $CoPS_3$ is a hole-dominant conductor. We observed the LMR in a wide range of magnetic fields. The LMR, the small volume reduction across the structural transition, and the previous theoretical prediction [33] suggest the coexistence of HS- and LS-Co^{2+} ions and the inhomogeneous magnetic moment distribution with a possible short-range magnetic ordering. Furthermore, the anomalous compression behavior of $V_{\text{f.u.}}$ and the pressure evolution of the electrical resistance and LMR suggest the possibility that the metallization occurs within the $P\bar{3}$ and the spin crossover completes up to 12 GPa, or the progress becomes moderate above the pressure in the $P\bar{3}$. By revealing the high-pressure phase and electrical transport property of $CoPS_3$, this paper summarizes the comprehensive

phase diagram of MPS_3 (M = V, Mn, Fe, Co, Ni, Cd) that metalize under compression. MPS_3 at ambient pressure has been an excellent platform for exploring emergent quantum phenomena due to their various electronic configurations. The phase diagram reveals that the electronic configurations at ambient pressure strongly influence the structural and electronic properties of MPS_3 at high pressures, making this series of compounds suitable platforms for exploring physical properties under compression.

ACKNOWLEDGMENTS

This research is funded by the Gordon and Betty Moore Foundation's EPiQS Initiative, Grant No. GBMF9069 to D.M. XRD experiments in this study were performed at GSECARS (Sector 13), Advanced Photon Source (APS), Argonne National Laboratory. GSECARS is supported by the National Science Foundation–Earth Sciences (EAR-1634415). This research used resources of the Advanced Photon Source, a U.S. Department of Energy (DOE) Office of Science User Facility operated for the DOE Office of Science by Argonne National Laboratory under Contract No. DE-AC02-06CH11357. Crystal growth and Raman characterization were performed under Air Force Office of Scientific Research (AFOSR) Grant No. LRIR 23RXCOR003 and AOARD-MOST Grant No. F4GGA21207H002. A part of the XRD experiment was supported by COMPRES under NSF Cooperative Agreement No. EAR-1606856. We thank Dr. Antonio M. dos Santos and Professor Maik Lang for providing us with the DACs for the XRD measurements. We thank Professor Heung-Sik Kim and Dr. Sungmo Kang for the fruitful comments and discussions.

[1] M. A. Susner, M. Chyasnavichyus, M. A. McGuire, P. Ganesh, and P. Maksymovych, Metal thio- and selenophosphates as multifunctional van der Waals layered materials, Adv. Mater. **29**, 1602852 (2017).

[2] M. Zhu, H. Kou, K. Wang, H. Wu, D. Ding, G. Zhou, and S. Ding, Promising functional two-dimensional lamellar metal thiophosphates: synthesis strategies, properties and applications, Mater. Horizons **7**, 3131 (2020).

[3] A. R. Wildes, V. Simonet, E. Ressouche, R. Ballou, and G. J. McIntyre, The magnetic properties and structure of the quasi-two-dimensional antiferromagnet $CoPS_3$, J. Phys.: Condens. Matter **29**, 455801 (2017).

[4] M. J. Coak, D. M. Jarvis, H. Hamidov, A. R. Wildes, J. A. M. Paddison, C. Liu, C. R. S. Haines, N. T. Dang, S. E. Kichanov, B. N. Savenko, S. Lee, M. Kratochvílová, S. Klotz, T. C. Hansen, D. P. Kozlenko, J.-G. Park, and S. S. Saxena, Emergent Magnetic Phases in Pressure-Tuned Van Der Waals Antiferromagnet $FePS_3$, Phys. Rev. X **11**, 011024 (2021).

[5] A. R. Wildes, S. J. Kennedy, and T. J. Hicks, True two-dimensional magnetic ordering in $MnPS_3$, J. Phys.: Condens. Matter **6**, L335 (1994).

[6] A. R. Wildes, V. Simonet, E. Ressouche, G. J. McIntyre, M. Avdeev, E. Suard, S. A. J. Kimber, D. Lançon, G. Pepe, B. Moubaraki, and T. J. Hicks, Magnetic structure of the quasi-two-dimensional antiferromagnet $NiPS_3$, Phys. Rev. B **92**, 224408 (2015).

[7] H.-S. Kim, K. Haule, and D. Vanderbilt, Mott Metal-Insulator Transitions in Pressurized Layered Trichalcogenides, Phys. Rev. Lett. **123**, 236401 (2019).

[8] X. Li, T. Cao, Q. Niu, J. Shi, and J. Feng, Coupling the valley degree of freedom to antiferromagnetic order, Proc. Natl. Acad. Sci. **110**, 3738 (2013).

[9] P. A. Joy and S. Vasudevan, Magnetism in the layered transition-metal thiophosphates MPS_3 (M = Mn, Fe, and Ni), Phys. Rev. B **46**, 5425 (1992).

[10] D. Lançon, H. C. Walker, E. Ressouche, B. Ouladdiaf, K. C. Rule, G. J. McIntyre, T. J. Hicks, H. M. Rønnow, and A. R. Wildes, Magnetic structure and magnon dynamics of the quasi-two-dimensional antiferromagnet $FePS_3$, Phys. Rev. B **94**, 214407 (2016).

[11] A. R. Wildes, H. M. Rønnow, B. Roessli, M. J. Harris, and K. W. Godfrey, Static and dynamic critical properties of the quasi-two-dimensional antiferromagnet $MnPS_3$, Phys. Rev. B **74**, 094422 (2006).

[12] M. J. Coak, S. Son, D. Daisenberger, H. Hamidov, C. R. S. Haines, P. L. Alireza, A. R. Wildes, C. Liu, S. S. Saxena, and J.-G. Park, Isostructural Mott transition in 2D honeycomb antiferromagnet $V_{0.9}PS_3$, npj Quantum Mater. **4**, 38 (2019).

[13] Y. Wang, Z. Zhou, T. Wen, Y. Zhou, N. Li, F. Han, Y. Xiao, P. Chow, J. Sun, M. Pravica, A. L. Cornelius, W. Yang, and Y. Zhao, Pressure-driven cooperative spin-crossover, large-volume collapse, and semiconductor-to-metal transition in manganese(II) honeycomb lattices, J. Am. Chem. Soc. **138**, 15751 (2016).

[14] Y. Wang, J. Ying, Z. Zhou, J. Sun, T. Wen, Y. Zhou, N. Li, Q. Zhang, F. Han, Y. Xiao, P. Chow, W. Yang, V. V. Struzhkin, Y. Zhao, and H.-K. Mao, Emergent superconductivity in an iron-based honeycomb lattice initiated by pressure-driven spin-crossover, Nat. Commun. **9**, 1914 (2018).

[15] C. R. S. Haines, M. J. Coak, A. R. Wildes, G. I. Lampronti, C. Liu, P. Nahai-Williamson, H. Hamidov, D. Daisenberger, and S. S. Saxena, Pressure-Induced Electronic and Structural Phase Evolution in the Van Der Waals Compound $FePS_3$, Phys. Rev. Lett. **121**, 266801 (2018).

[16] T. Matsuoka, A. Haglund, R. Xue, J. S. Smith, M. Lang, A. M. dos Santos, and D. Mandrus, Pressure-induced insulator-metal transition in two-dimensional Mott insulator $NiPS_3$, J. Phys. Soc. Jpn. **90**, 124706 (2021).

[17] X. Ma, Y. Wang, Y. Yin, B. Yue, J. Dai, J. Cheng, J. Ji, F. Jin, F. Hong, J.-T. Wang, Q. Zhang, and X. Yu, Dimensional crossover tuned by pressure in layered magnetic $NiPS_3$, Sci. China Phys. Mech. Astron. **64**, 297011 (2021).

[18] N. C. Harms, H.-s. Kim, A. J. Clune, K. A. Smith, K. R. O'Neal, A. V. Haglund, D. G. Mandrus, Z. Liu, K. Haule, D. Vanderbilt, and J. L. Musfeldt, Piezochromism in the magnetic chalcogenide $MnPS_3$, npj Quantum Mater. **5**, 56 (2020).

[19] R. Rao, B. S. Conner, R. Selhorst, and M. A. Susner, Pressure-driven phase transformations and phase segregation in ferrielectric $CuInP_2S_6$-$In_{4/3}P_2S_6$ self-assembled heterostructures, Phys. Rev. B **104**, 235421 (2021).

[20] M. Niu, H. Cheng, X. Li, J. Yu, X. Yang, Y. Gao, R. Liu, Y. Cao, K. He, X. Xie, Q. Shen, M. Lu, L. Wang, T. Yin, and J. Yan, Pressure-induced phase transitions in weak interlayer coupling $CdPS_3$, Appl. Phys. Lett. **120**, 233104 (2022).

[21] N. C. Harms, K. A. Smith, A. V. Haglund, D. G. Mandrus, Z. Liu, H.-s. Kim, and J. L. Musfeldt, Metal site substitution and role of the dimer on symmetry breaking in $FePS_3$ and $CrPS_4$ under pressure, ACS Appl. Electron. Mater. **4**, 3246 (2022).

[22] G. Ouvrard, R. Fréour, R. Brec, and J. Rouxel, A mixed valence compound in the two dimensional MPS_3 family: $V_{0.78}PS_3$ structure and physical properties, Mater. Res. Bull. **20**, 1053 (1985).

[23] G. Ouvrard, R. Brec, and J. Rouxel, Structural determination of some MPS_3 layered phases (M = Mn, Fe, Co, Ni and Cd), Mater. Res. Bull. **20**, 1181 (1985).

[24] M. J. Coak, D. M. Jarvis, H. Hamidov, C. R. Haines, P. L. Alireza, C. Liu, S. Son, I. Hwang, G. I. Lampronti, D. Daisenberger, P. Nahai-Williamson, A. R. Wildes, S. S. Saxena, and J. G. Park, Tuning dimensionality in van-der-Waals antiferromagnetic Mott insulators $TMPS_3$, J. Phys.: Condens. Matter **32**, 124003 (2020).

[25] N. C. Harms, T. Matsuoka, S. Samanta, A. J. Clune, K. A. Smith, A. V. Haglund, E. Feng, H. Cao, J. S. Smith, D. G. Mandrus, H.-s. Kim, Z. Liu, and J. L. Musfeldt, Symmetry progression and possible polar metallicity in $NiPS_3$ under pressure, npj 2D Mater. Appl. **6**, 40 (2022).

[26] E. Ressouche, M. Loire, V. Simonet, R. Ballou, A. Stunault, and A. Wildes, Magnetoelectric $MnPS_3$ as a candidate for ferrotoroidicity, Phys. Rev. B **82**, 100408(R) (2010).

[27] A. Bhutani, J. L. Zuo, R. D. McAuliffe, C. R. dela Cruz, and D. P. Shoemaker, Strong anisotropy in the mixed antiferromagnetic system $Mn_{1-x}Fe_xPSe_3$, Phys. Rev. Mater. **4**, 034411 (2020).

[28] A. Wiedenmann, J. Rossat-Mignod, A. Louisy, R. Brec, and J. Rouxel, Neutron diffraction study of the layered compounds manganese selenophosphate ($MnPSe_3$) and iron selenophosphate ($FePSe_3$), Solid State Commun. **40**, 1067 (1981).

[29] K. C. Rule, G. J. McIntyre, S. J. Kennedy, and T. J. Hicks, Single-crystal and powder neutron diffraction experiments on $FePS_3$: Search for the magnetic structure., Phys. Rev. B: Condens. Matter Mater. Phys. **76**, 134402 (2007).

[30] K. Ichimura and M. Sano, Electrical conductivity of layered transition-metal phosphorus trisulfide crystals, Synth. Met. **45**, 203 (1991).

[31] G. Le Flem, R. Brec, G. Ouvard, A. Louisy, and P. Segransan, Magnetic interactions in the layer compounds MPX_3 (M = Mn, Fe, Ni; X = S, Se), J. Phys. Chem. Solids **43**, 455 (1982).

[32] G. Ouvrard, R. Brec, and J. Rouxel, Synthesis and physical characterization of the lamellar compound $CoPS_3$, C. R. Acad. Sci., Ser. II **294**, 971 (1982).

[33] Y. Gu, S. Zhang, and X. Zou, Tunable magnetism in layered $CoPS_3$ by pressure and carrier doping, Sci. Chin. Mater. **64**, 673 (2021).

[34] A. F. May, J. Yan, and M. A. McGuire, A practical guide for crystal growth of van der Waals layered materials, J. Appl. Phys. **128**, 051101 (2020).

[35] H. K. Mao, J. Xu, and P. M. Bell, Calibration of the ruby pressure gauge to 800 kbar under quasi-hydrostatic conditions, J. Geophys. Res. **91**, 4673 (1986).

[36] See Supplemental Materials at http://link.aps.org/supplemental/10.1103/PhysRevB.107.165125 for the experimental setups, XRD images, the equation states, Gruneisen parameters, and Raman scattering spectra analysis, this includes Ref. [80].

[37] C. Prescher and V. B. Prakapenka, DIOPTAS: A program for reduction of two-dimensional X-ray diffraction data and data exploration, High Press. Res. **35**, 223 (2015).

[38] Y. Seto, D. Nishio-Hamane, T. Nagai, and N. Sata, Development of a software suite on x-ray diffraction experiments, Rev. High Pressure Sci. Technol. **20**, 269 (2010).

[39] R. D. Shannon, Revised effective ionic radii and systematic studies of interatomic distances in halides and chalcogenides, Acta Crystallogr. Sec. A **32**, 751 (1976).

[40] Q. Liu, L. Wang, Y. Fu, X. Zhang, L. Huang, H. Su, J. Lin, X. Chen, D. Yu, X. Cui, J.-W. Mei, and J.-F. Dai, Magnetic order in XY-type antiferromagnetic monolayer $CoPS_3$ revealed by Raman spectroscopy, Phys. Rev. B **103**, 235411 (2021).

[41] S. Klotz, J.-C. Chervin, P. Munsch, and G. Le Marchand, Hydrostatic limits of 11 pressure transmitting media, J. Phys. D **42**, 075413 (2009).

[42] I. Fujishiro, G. Piermarini, S. Block, and R. Munro, Viscosities and glass transition pressure in the methanol-ethanol-water system, in *Proceedings of the 8th AIRAPT and 19th EHPRG Conference*, edited by C.-M. Backman, T. Johannisson, and L. Tengnér (Arkitektkopia, University of Uppsala, Sweden, 1982), Vol. II, p. 608.

[43] N. Tateiwa and Y. Haga, Evaluations of pressure-transmitting media for cryogenic experiments with diamond anvil cell, Rev. Sci. Instrum. **80**, 123901 (2009).

[44] K. Momma and F. Izumi, VESTA 3 for three-dimensional visualization of crystal, volumetric and morphology data, J. Appl. Crystallogr. **44**, 1272 (2011).

[45] L. Savary, Transverse transport, Nat. Phys. **14**, 1073 (2018).

[46] I. M. Lifshits, M. I. Azbel, and M. I. Kaganov, The theory of galvanomagnetic effects in metals, Soviet Physics Jetp-Ussr **4**, 41 (1957).

[47] J. M. Ziman, Galvanomagnetic properties of cylindrical fermi surfaces, Philos. Mag. **3**, 1117 (1958).

[48] Y. Feng, Y. Wang, D. M. Silevitch, J.-Q. Yan, R. Kobayashi, M. Hedo, T. Nakama, Y. nuki, A. V. Suslov, B. Mihaila, P. B. Littlewood, and T. F. Rosenbaum, Linear magnetoresistance in the low-field limit in density-wave materials, Proc. Natl. Acad. Sci. **116**, 11201 (2019).

[49] B. Chen, J. M. Jackson, W. Sturhahn, D. Zhang, J. Zhao, J. K. Wicks, and C. A. Murphy, Spin crossover equation of state and sound velocities of $(Mg_{0.65}Fe_{0.35})O$ ferropericlase to 140 GPa, J. Geophys. Res. Solid Earth **117**, B082081 (2012).

[50] E. Greenberg, W. M. Xu, M. Nikolaevsky, E. Bykova, G. Garbarino, K. Glazyrin, D. G. Merkel, L. Dubrovinsky, M. P. Pasternak, and G. K. Rozenberg, High-pressure magnetic, electronic, and structural properties of MFe_2O_4 (M = Mg, Zn, Fe) ferric spinels, Phys. Rev. B **95**, 195150 (2017).

[51] G. K. Rozenberg, M. P. Pasternak, W. M. Xu, L. S. Dubrovinsky, S. Carlson, and R. D. Taylor, Consequences of pressure-instigated spin crossover in $RFeO_3$ perovskites; a volume collapse with no symmetry modification, Europhys. Lett. **71**, 228 (2005).

[52] J. Wang, A. M. DaSilva, C.-Z. Chang, K. He, J. K. Jain, N. Samarth, X.-C. Ma, Q.-K. Xue, and M. H. W. Chan, Evidence for electron-electron interaction in topological insulator thin films, Phys. Rev. B **83**, 245438 (2011).

[53] Y. Zhao, C.-Z. Chang, Y. Jiang, A. DaSilva, Y. Sun, H. Wang,

Y. Xing, Y. Wang, K. He, X. Ma, Q.-K. Xue, and J. Wang, Demonstration of surface transport in a hybrid Bi_2Se_3/Bi_2Te_3 heterostructure, Sci. Rep. **3**, 3060 (2013).

[54] H. Tang, D. Liang, R. L. J. Qiu, and X. P. a. Gao, Two-dimensional transport-induced linear magneto-resistance in topological insulator Bi_2Se_3 nanoribbons, ACS Nano **5**, 7510 (2011).

[55] C. M. Wang and X. L. Lei, Linear magnetoresistance on the topological surface, Phys. Rev. B **86**, 035442 (2012).

[56] G. M. Gusev, E. B. Olshanetsky, Z. D. Kvon, N. N. Mikhailov, and S. A. Dvoretsky, Linear magnetoresistance in HgTe quantum wells, Phys. Rev. B **87**, 081311(R) (2013).

[57] X. Wang, Y. Du, S. Dou, and C. Zhang, Room Temperature Giant and Linear Magnetoresistance in Topological Insulator Bi_2Te_3 Nanosheets, Phys. Rev. Lett. **108**, 266806 (2012).

[58] M. Novak, S. Sasaki, K. Segawa, and Y. Ando, Large linear magnetoresistance in the Dirac semimetal TlBiSSe, Phys. Rev. B **91**, 041203(R) (2015).

[59] T. Liang, Q. Gibson, M. N. Ali, M. Liu, R. J. Cava, and N. P. Ong, Ultrahigh mobility and giant magnetoresistance in the Dirac semimetal Cd_3As_2, Nat. Mater. **14**, 280 (2015).

[60] Y. Zhao, H. Liu, C. Zhang, H. Wang, J. Wang, Z. Lin, Y. Xing, H. Lu, J. Liu, Y. Wang, S. M. Brombosz, Z. Xiao, S. Jia, X. C. Xie, and J. Wang, Anisotropic Fermi Surface and Quantum Limit Transport in High Mobility Three-Dimensional Dirac Semimetal Cd_3As_2, Phys. Rev. X **5**, 031037 (2015).

[61] J. Feng, Y. Pang, D. Wu, Z. Wang, H. Weng, J. Li, X. Dai, Z. Fang, Y. Shi, and L. Lu, Large linear magnetoresistance in Dirac semimetal Cd_3As_2 with Fermi surfaces close to the Dirac points, Phys. Rev. B **92**, 081306(R) (2015).

[62] C. Shekhar, A. K. Nayak, Y. Sun, M. Schmidt, M. Nicklas, I. Leermakers, U. Zeitler, Y. Skourski, J. Wosnitza, Z. Liu, Y. Chen, W. Schnelle, H. Borrmann, Y. Grin, C. Felser, and B. Yan, Extremely large magnetoresistance and ultrahigh mobility in the topological Weyl semimetal candidate NbP, Nat. Phys. **11**, 645 (2015).

[63] Y. Zhao, H. Liu, J. Yan, W. An, J. Liu, X. Zhang, H. Wang, Y. Liu, H. Jiang, Q. Li, Y. Wang, X.-Z. Li, D. Mandrus, X. C. Xie, M. Pan, and J. Wang, Anisotropic magnetotransport and exotic longitudinal linear magnetoresistance in WTe_2 crystals, Phys. Rev. B **92**, 041104(R) (2015).

[64] R. Xu, A. Husmann, T. F. Rosenbaum, M.-L. Saboungi, J. E. Enderby, and P. B. Littlewood, Large magnetoresistance in non-magnetic silver chalcogenides, Nature (London) **390**, 57 (1997).

[65] W. Zhang, R. Yu, W. Feng, Y. Yao, H. Weng, X. Dai, and Z. Fang, Topological Aspect and Quantum Magnetoresistance of β-Ag_2Te, Phys. Rev. Lett. **106**, 156808 (2011).

[66] A. A. Sinchenko, P. D. Grigoriev, P. Lejay, and P. Monceau, Linear magnetoresistance in the charge density wave state of quasi-two-dimensional rare-earth tritellurides, Phys. Rev. B **96**, 245129 (2017).

[67] T. Khouri, U. Zeitler, C. Reichl, W. Wegscheider, N. E. Hussey, S. Wiedmann, and J. C. Maan, Linear Magnetoresistance in a Quasifree Two-Dimensional Electron Gas in an Ultrahigh Mobility GaAs Quantum Well, Phys. Rev. Lett. **117**, 256601 (2016).

[68] A. A. Abrikosov, Quantum magnetoresistance, Phys. Rev. B **58**, 2788 (1998).

[69] A. A. Abrikosov, Quantum linear magnetoresistance, Europhys. Lett. **49**, 789 (2000).

[70] R. A. Young, Influence of localized Umklapp scattering on the galvanomagnetic properties of metals, Phys. Rev. **175**, 813 (1968).

[71] M. Naito and S. Tanaka, Galvanomagnetic effects in the charge-density-wave state of 2H-$NbSe_2$ and 2H-$TaSe_2$, J. Phys. Soc. Jpn. **51**, 228 (1982).

[72] J. C. W. Song, G. Refael, and P. A. Lee, Linear magnetoresistance in metals: Guiding center diffusion in a smooth random potential, Phys. Rev. B **92**, 180204(R) (2015).

[73] M. M. Parish and P. B. Littlewood, Non-saturating magnetoresistance in heavily disordered semiconductors, Nature (London) **426**, 162 (2003).

[74] J. Hu and T. F. Rosenbaum, Classical and quantum routes to linear magnetoresistance, Nat. Mater. **7**, 697 (2008).

[75] B. Raquet, M. Viret, P. Warin, E. Sondergard, and R. Mamy, Negative high field magnetoresistance in 3d ferromagnets, Phys. B: Condens. Matter **294-295**, 102 (2001).

[76] Q. Wang, W. Zhang, W. Chen, Y. Xing, Y. Sun, Z. Wang, J.-W. Mei, Z. Wang, L. Wang, X.-C. Ma, F. Liu, Q.-K. Xue, and J. Wang, Spin fluctuation induced linear magnetoresistance in ultrathin superconducting FeSe films, 2D Mater. **4**, 034004 (2017).

[77] W. Pan, J. S. Xia, H. L. Stormer, D. C. Tsui, C. L. Vicente, E. D. Adams, N. S. Sullivan, L. N. Pfeiffer, K. W. Baldwin, and K. W. West, Quantization of the Diagonal Resistance: Density Gradients and the Empirical Resistance Rule in a 2D System, Phys. Rev. Lett. **95**, 066808 (2005).

[78] S. H. Simon and B. I. Halperin, Explanation for the Resistivity Law in Quantum Hall Systems, Phys. Rev. Lett. **73**, 3278 (1994).

[79] E. Prouzet, G. Ouvrard, and R. Brec, Structure determination of $ZnPS_3$, Mater. Res. Bull. **21**, 195 (1986).

[80] F. D. Stacey and J. H. Hodgkinson, Thermodynamics with the Grüneisen parameter: Fundamentals and applications to high pressure physics and geophysics, Phys. Earth Planet. Inter. **286**, 42 (2019).